RSC Advances

PAPER

View Article Online
View Journal | View Issue

Cite this: *RSC Adv.*, 2024, **14**, 36437

A new herbal extract carbon nanodot nanomedicine for anti-renal cell carcinoma through the PI3K/AKT signaling pathway†

Ning Tian,[a] Xiangling Liu,[a] Xiaoyu He,[a] Ying Liu,[a] Lizhi Xiao,[a] Penghui Wang,[a] Di Zhang,[a] Zhe Zhang,[a] Yu Zhao, *[a] Quan Lin, [c] Changkui Fu*[b] and Yingnan Jiang *[ab]

New Re carbon nanodots with narrow size distribution, good water solubility and high cell membrane permeability were prepared from a herbal extract. They exhibited high inhibitory effects on renal cancer A498 cells and renal cell carcinoma. They could stimulate the production of ROS, induce mitochondrial dysfunction, and accelerate the release of intracellular calcium ions in the A498 cells. Transcriptomic tests were performed on A498 cells after administration, and the results were analyzed by qPCR and immunofluorescence. The results suggested that the Re carbon nanodots could downregulate the abnormally activated PI3K/AKT signaling pathway and perform cell cycle arrest in the S phase along with the inhibition of cell proliferation. Finally, in conjunction with the abnormal mitochondrial function, the Re carbon nanodots could ultimately promote the apoptosis of the A498 cells. *In vivo* tumor-bearing mouse experiments further showed that the Re carbon nanodots had a strong inhibitory effect on xenograft kidney cancer tumors. The prepared Re carbon nanodots have good anti-renal cancer A498 cell and renal cell carcinoma bioactivity and are expected to be a potential drug for the treatment of kidney cancer with low toxicity and high safety.

Received 6th October 2024
Accepted 30th October 2024

DOI: 10.1039/d4ra07181f

rsc.li/rsc-advances

Introduction

With the rapid development of modern medical technology, the survival of many cancer patients has improved. However, cancer still remains a huge challenge for human health worldwide. Among the cancers of the renal system, kidney tumors account for a large proportion, and more than 90% of kidney tumors are renal cell carcinomas. Due to the low sensitivity of kidney cancer to chemotherapy drugs, besides the resection surgery, immunotherapy (such as PD-1 antibody) can also prevent the proliferation and spread of kidney tumors.[1,2] However, owing to the complex interactions in the tumor microenvironment, immunotherapy often triggers strong side effects and even the emergence of diseases such as immune encephalitis.[3] Thus, the use of immunotherapy drugs is also a major challenge for the treatment of kidney cancer. Based on this, there is an urgent need to develop highly effective drugs with low toxicity for the treatment of kidney cancer that improve the patients' clinical treatment feelings, compliance and treatment effects and prolong the survival of patients.

Numerous natural herbs and their extracts (including a variety of ginsenosides) have high medicinal value due to their high biological activity and extremely low biological toxicity for a long time.[4,5] However, due to their structure and low water solubility, cell uptake of most of the natural medicines is low.[6] This bioavailability prevents them from fully exerting the medicinal effects and greatly limits the clinical application. In the field of nanomedicine technology, a large number of studies have confirmed that nanomedicine can be taken up by cells in large quantities through endocytosis due to its unique size and modifiable surface properties.[7–9] Therefore, the development and innovation of appropriate low biotoxicity nanomedicine delivery systems will greatly improve the bioavailability of many natural medicines and their extracts and help them to exert the best therapeutic effect. Among many nanomedicine delivery systems, carbon nanodots (CDs) have high drug delivery potential owing to their numerous precursor types, extremely low biological toxicity, uniform size distribution, good water solubility, and designable biological activity.[10,11] In recent years, some studies have found that CDs prepared from precursors with certain biological activity could combine the advantages of both partial active structure of the original precursors and their own nanostructures. For example, Li *et al.* used fresh tender

[a]*Jilin Ginseng Academy, Changchun University of Chinese Medicine, Changchun 130117, P. R. China. E-mail: jiangyn@ccucm.edu.cn; cnzhaoyu1972@126.com*
[b]*Australian Institute for Bioengineering and Nanotechnology, The University of Queensland, Brisbane, Queensland 4072, Australia. E-mail: changkui.fu@uq.edu.au*
[c]*State Key Laboratory of Supramolecular Structure and Materials, College of Chemistry, Jilin University, Changchun 130012, P. R. China*

† Electronic supplementary information (ESI) available. See DOI: https://doi.org/10.1039/d4ra07181f

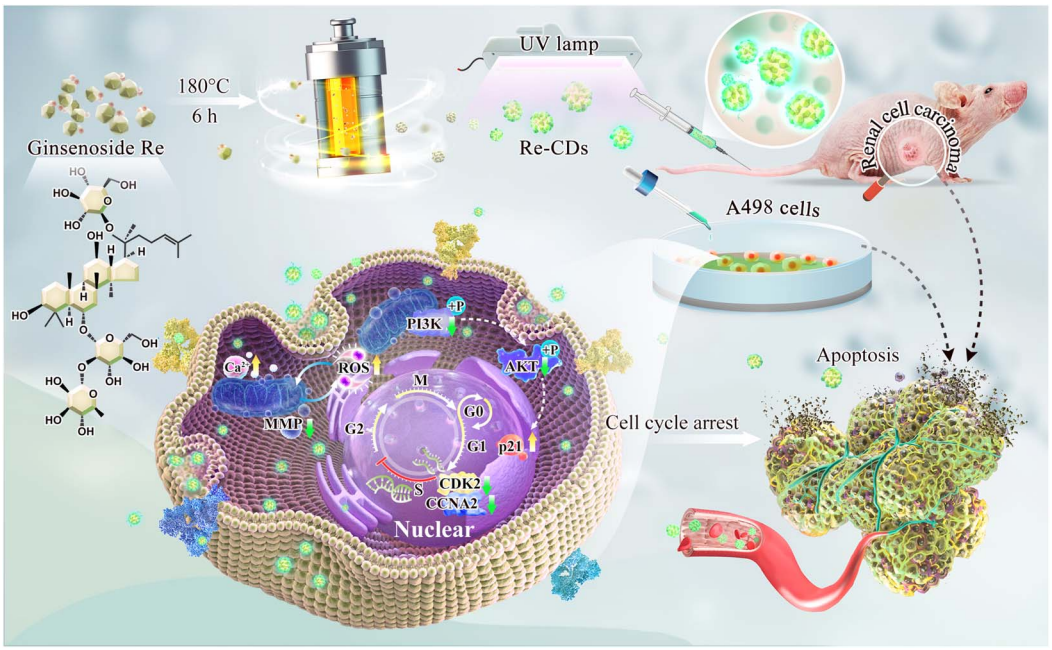

Scheme 1 Schematic of the synthesis route of the Re-CDs and its anti-renal cancer A498 cell and renal cell carcinoma bioactivity.

ginger juice as the precursor. The obtained ginger CDs had low to normal cytotoxicity, and a selective inhibitory effect on human hepatoma cells HepG2. The results showed that the ginger CDs could upregulate p53 proteins and induce the production of intracellular ROS, thereby exerting the therapeutic effect of promoting the apoptosis of tumor cells. Tian *et al.* used three pentacyclic triterpenoids (PTs), including glycyrrhetinic acid (GA), ursolic acid (UA) and oleanolic acid (OA), as precursors to fabricate CDs under hydrothermal condition. The obtained CDs had an anti-human colon cancer cell HCT116 effect by mitochondrial targeting function. Jiang *et al.* used the total ginsenosides as a precursor to prepare GS-CDs. The results showed that the GS-CDs had very low toxicity and animal side effects, with a good inhibitory effect on human neuroblastoma cells and human neuroblastoma. Increasingly more nanomedicines of CDs based on natural drugs are being developed, which have shown good application prospects in the treatment of cancer. These CDs exhibit more significant anti-cancer effects compared to their raw materials. The mechanism (apoptosis, ferroptosis, and autophagy) of inducing cell death is usually similar to that of the raw materials.[12–14] However, because of the numerous types of cancer, rapid deterioration and metastasis of tumors, and strong toxic side effects of drugs in clinical treatment, it is still necessary to continue exploring new CDs drugs with good therapeutic effects to meet practical needs.

Phosphatidylinositol 3-kinase/protein kinase B (PI3K/AKT) is one of the highly conserved signal transduction pathways in eukaryotic cells, and is also one of the most commonly deregulated pathways in cancer.[15–17] The PI3K/AKT signaling pathway exhibits abnormal regulation in a variety of malignant tumors, which in turn would promote tumor cell proliferation and neovascularization, inhibit tumor cell apoptosis, and be closely related to tumor invasion and metastasis.[18–26] Inhibition of the PI3K/AKT signaling pathway would trigger and accelerate cell cycle arrest and apoptosis of cancer cells, and effectively inhibit the development of cancer. Therefore, inhibition of the PI3K/AKT signaling pathway is intended to be one approach for the treatment of tumors.

In this study, new Re-carbon nanodots (Re-CDs) have been synthesized by a hydrothermal method with ginsenoside Re, a natural plant active monomer, as the only precursor. The Re-CDs have uniform size distribution, good water solubility, low biotoxicity and high cell membrane permeability, and have shown a high inhibitory effect on both kidney cancer A498 cells and kidney cancer *in vitro* and *in vivo*. The molecular mechanisms of the Re-CDs anti-A498 cells have been revealed at the cellular level through transcriptomics testing, qPCR validation, and immunofluorescence testing. The results showed that the Re-CDs promoted cycle arrest and apoptosis of the A498 cells through the PI3K/AKT signaling pathway. This study would provide a new research strategy based on CD nanomedicine for anti-kidney cancer treatment in the future Scheme 1.

Results and discussion

Firstly, the properties and structures of the prepared Re-CDs were characterized and analyzed (Fig. 1). The solubility of the Re monomer in water is poor.[27] However, the prepared Re-CDs have good solubility in water. Under normal light, the Re methanol solution (500 μg mL^{-1}) is faint and transparent, and the Re-CDs aqueous solution (500 μg mL^{-1}) is transparent and yellowish. Under UV light irradiation of 365 nm, the Re solution shows little fluorescence emission, while the Re-CDs solution shows an obvious blue-green fluorescence (Fig. 1A and S1†). Fluorescence spectra show that the Re-CDs have obvious excitation-dependent characteristics. Their optimal excitation

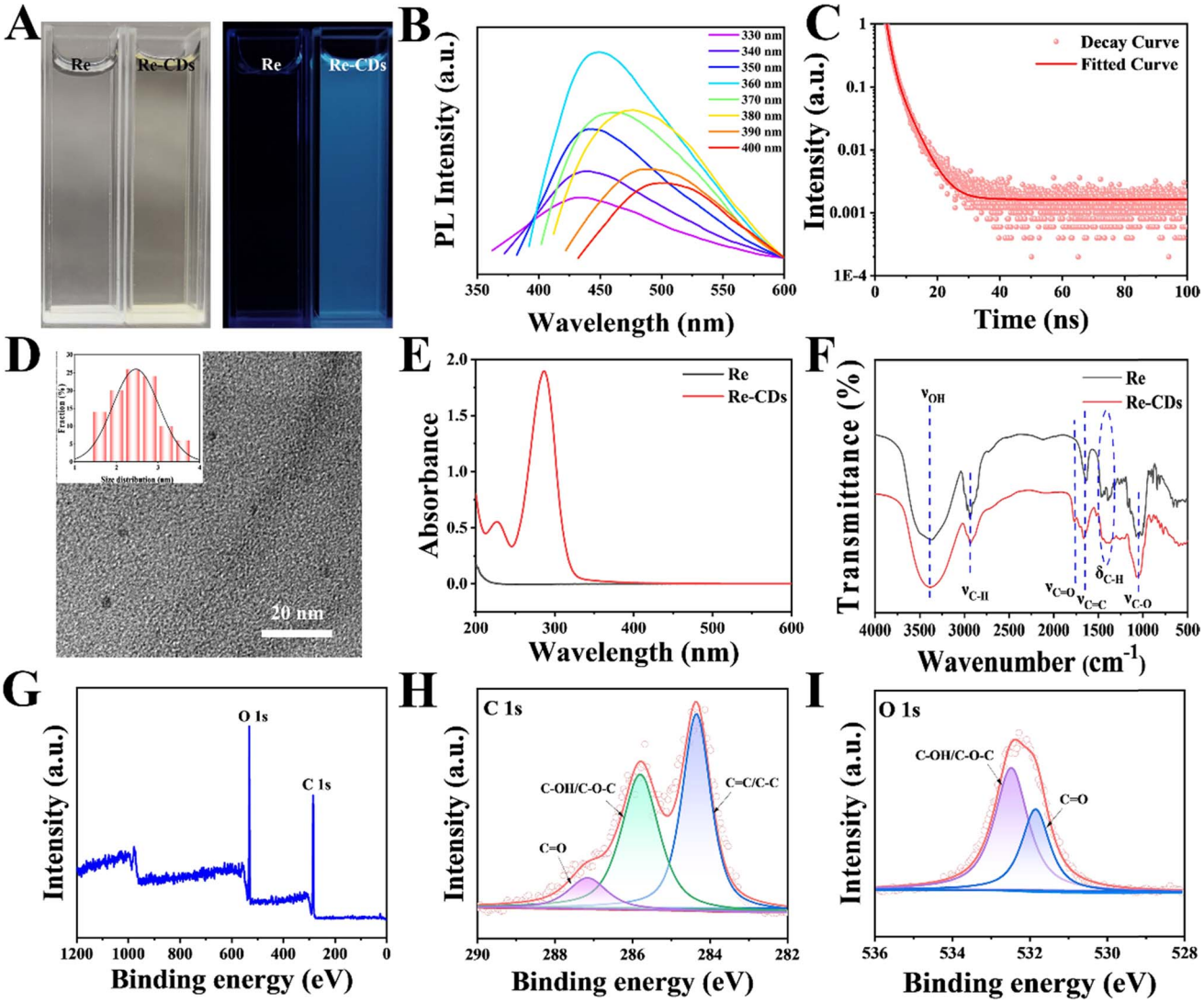

Fig. 1 Characterization of the Re-CDs. (A) Photograph of the Re (0.5 mg mL^{-1}) methanol solution (left) and the Re-CDs (0.5 mg mL^{-1}) aqueous solution (right) under normal light and UV light of 365 nm. (B) Fluorescence spectra of the Re-CDs (0.45 mg mL^{-1}). (C) Fluorescence decay curve of the Re-CDs (0.5 mg mL^{-1}). (D) TEM image of the Re-CDs (0.5 mg mL^{-1}) and the particle size distribution (top left). The scale bar is 20 nm. (E) UV spectra of the Re (0.03 mg mL^{-1}) in methanol and the Re-CDs (0.03 mg mL^{-1}) aqueous solution. (F) FTIR spectra of the Re (20 mg) and the Re-CDs (20 mg). (G) XPS spectra of the Re-CDs (20 mg), including the high-resolution C 1s (H) and O 1s (I) spectra.

wavelength is ~360 nm and the optimal emission wavelength is ~450 nm (Fig. 1B). The third-order decay exponential function was fitted according to the fluorescence decay curve of the Re-CDs, and three fluorescence lifetimes (τ) were obtained. The results show that the Re-CDs have three fluorescence centers and an average fluorescence lifetime of 1.49 ns (Fig. 1C and Table S1†). The quantum yield of the Re-CDs is ~3.6%. TEM photographs show that the Re-CDs are uniform in size and have good dispersion. The diameter distribution is between 1–4 nm, and mainly concentrated at ~2.5 nm (Table S2†). The clear non-dotted rings formed in the selected area electron diffraction (SAED) showed that the prepared Re-CDs had a small lattice structure (Fig. 1D and S2†). The UV spectra showed that there is no significant absorption peak in the Re solution. Meanwhile, two distinct absorption peaks appear at ~226 nm and ~287 nm in the Re-CDs solution (Fig. 1E) due to the π–π^* and n–π^* transitions, respectively.[28] Compared with the original Re molecule, the prepared Re-CDs clearly exhibited new strong fluorescent emission and UV absorption, which are supposed to be caused by the cross-linking of the ginsenoside Re molecules under high temperature and high pressure during the hydrothermal reaction. The cross-linking led to the obstruction of vibrational and rotational motion between the Re molecules, resulting in the cross-linked enhanced emission (CEE) effect within the final prepared Re-CDs.[14,29]

For the Fourier transform infrared (FTIR) spectra (Fig. 1F), the Re-CDs exhibit many absorption peaks that are similar to those of the Re molecule, including the O–H (3409 cm^{-1}), C–H (2942 cm^{-1}), C=C (1659 cm^{-1}) and C–O (1046 cm^{-1}) stretching bands. Additionally, the Re-CDs show a new absorption peak at 1767 cm^{-1} compared to the Re molecule. This may be caused by the expansion and contraction vibration of C=O on the surface

of the Re-CDs. The appearance of the new absorption peak suggests that besides retaining many active groups of the Re molecule, new hydrophilic functional groups appear during the formation of the Re-CDs. The X-ray photoelectron spectroscopy (XPS) analysis shows the two major absorption peaks of C and O of the Re-CDs (Fig. 1G). The high-resolution C 1s spectrum can be deconvoluted to three peaks, a C=C bond at ~284.3 eV, a C–O/C–O–C bond at ~285.7 eV and a C=O band at ~287.1 eV (Fig. 1H). The high-resolution O 1s spectrum can be deconvoluted to two peaks, a main C–O/C–O–C bond at ~532.4 eV and a C=O bond at ~531.8 eV (Fig. 1I). The FTIR and XPS spectral results show that the synthesized Re-CDs retain a certain active structure of the raw material, with the emergence of new hydrophilic groups on the surface and higher water solubility.[13]

In addition, the stability of the Re-CDs has been investigated under UV irradiation, different temperatures, different pH and different salt ion concentrations (NaCl and KCl). The results show that the Re-CDs possess good stability under these different conditions (Fig. S3†). It implies that as a potential drug, the Re-CDs have a good application basis for use and storage.

The *in vitro* biological activity of the Re-CDs has been preliminarily investigated (Fig. 2). The Re dissolved in DMSO solution at different concentrations (0, 30, 50, 70, and 90 μg mL^{-1}) showed little inhibitory effect on the A498 cells (Fig. 2A). Meanwhile, the Re-CDs of different concentrations (0, 30, 50, 70, and 90 μg mL^{-1}) showed clear inhibitory activity against A498 cell proliferation in a dose-dependent manner (Fig. 2B). At the highest administered concentration of 90 μg mL^{-1}, the viability rate of the A498 cells was only ~28.6% ± 1.3%. Considering the treatment of tumors, the Re-CDs have shown good inhibitory effect on the kidney tumor cells, compared to the carbon nanodots prepared *via* hydrothermal method from some other extracts that have been previously reported (Table S3†). The toxicity of the Re-CDs to the human normal hepatocytes (LO2) cells was much weaker under the same condition (Fig. 2C). At the dosing concentration of 90 μg mL^{-1}, the viability of the LO2 cells was ~85.9% ± 3.5%. The morphological results under the microscope showed that with the increase of the administration concentration of the Re-CDs, the morphological changes of the A498 cells (such as shrinkage and fragmentation) became more obvious (Fig. S4†). It is similar to the trend of cell suppression in Fig. 2B. In the hemolysis experiment, a large concentration range (50–500 μg mL^{-1}) of the Re-CDs would not cause red blood cell damage in mice (Fig. 2D). After incubation with 500 μg mL^{-1} of Re-CDs, the hemolysis rate was only ~3.1%. This suggests that the prepared Re-CDs have a good safety profile, which is beneficial for clinical application.[30]

Utilizing the fluorescence characteristics of the Re-CDs, the process and path of the Re-CDs into the A498 cells were observed by a fluorescence microscopy at different times and different temperatures (Fig. S5 and S6†). It can be seen that the Re-CDs were mainly concentrated in the cytoplasm after entering the cells. At 37 °C, the intracellular fluorescence intensity gradually increased with time at the beginning of the co-incubation (1–6 h). The fluorescence intensity reached the highest at ~6 h, indicating that a large number of Re-CDs had been taken up by the A498 cells at this time. With the further extension of the incubation time (8–36 h), the fluorescence intensity in the cells gradually decreased. It may be due to the fact that after the Re-CDs entered the cells, a part of them reacted with the cell substances causing their structure to be disrupted, and remaining were excreted from the cells through metabolism, resulting in a gradual decrease of the intracellular fluorescence intensity. At 48 h, the intracellular fluorescence almost disappeared. This diminished fluorescence is indicative of the time at which the severely damaged A498 cells showed almost stagnant physiological activities, such as intracellular material exchange and energy metabolism: the extracellular Re-CDs no longer entered the cells, and the intracellular Re-CDs were destroyed or metabolically eliminated. Meanwhile, at 4 °C, after co-incubating with the Re-CDs for 6 h, the A498 cells emitted weak fluorescence signal (Fig. S6†). This weak signal is possibly due to physiological activities (such as substance exchange and energy metabolism) in the A498 cells that were inhibited under the low temperature, resulting in a low uptake of the fluorescent Re-CDs. In contrast, the physiological activities of the A498 cells were normal at 37 °C. It had a large uptake of the Re-CDs, with a high intracellular fluorescence intensity. Combined with the previous reports on nanomedicine CDs, it further suggests that the Re-CDs are mainly taken up into the A498 cells through endocytosis.[14,31]

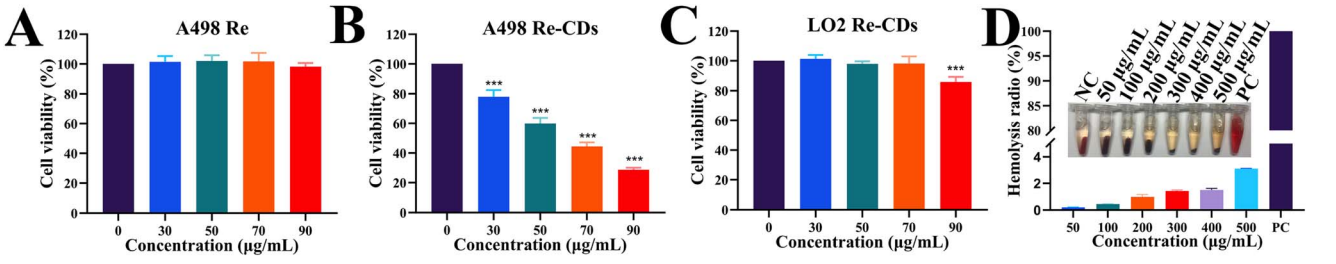

Fig. 2 Effect of the Re-CDs on cells *in vitro*. (A) Statistical diagram of the viability of the A498 cells at different concentrations of the Re in DMSO. (B) Statistical diagram of the viability of the A498 cells at different concentrations of the Re-CDs. (C) Statistical diagram of the viability of the LO2 cells at different concentrations of the Re-CDs. (D) Calculated histogram of the hemolysis rate and images of the red blood cells of mouse after co-incubation for 2 h with water (positive control, PC) (set as 100%), the Re-CDs of different concentrations (50, 100, 200, 300, 400 and 500 μg mL^{-1}), and the physiological saline (negative control, NC) at 37 °C. ***$p < 0.001$, compared to 0 μg mL^{-1}.

The effects of the Re-CDs on the proliferation and migration of the A498 cells were investigated by cell colony assay and cell migration assay (Fig. 3). The A498 cells was co-incubated with different concentrations of the Re-CDs for 48 h. Then the A498 cells was recultured for another 2 weeks and their colony formation was observed (Fig. 3A). Compared with the control group (Re-CDs, 0 μg mL^{-1}), the colony forming ability of the A498 cells was significantly inhibited ($p < 0.001$). At the administered concentration of 90 μg mL^{-1} of the Re-CDs, the colony generating capacity of the A498 cells decreased to ~24.9% ± 6.4% (Fig. 3F). The cell scratch assay was performed to investigate the changes of the lateral migration ability of the administered A498 cells (Fig. 3B). After 24 h of co-incubation with the Re-CDs, the lateral migration ability of the A498 cells was significantly inhibited, and showed a dose-dependent trend (Fig. 3B and G). Compared with the control group (Re-CDs, 0 μg mL^{-1}), the wound healing rate of the A498 cells was ~46.9% ± 7.9% at the Re-CDs administered concentration of 90 μg mL^{-1}. The changes in the longitudinal migration ability of the A498 cells after administration was detected by the cell transwell

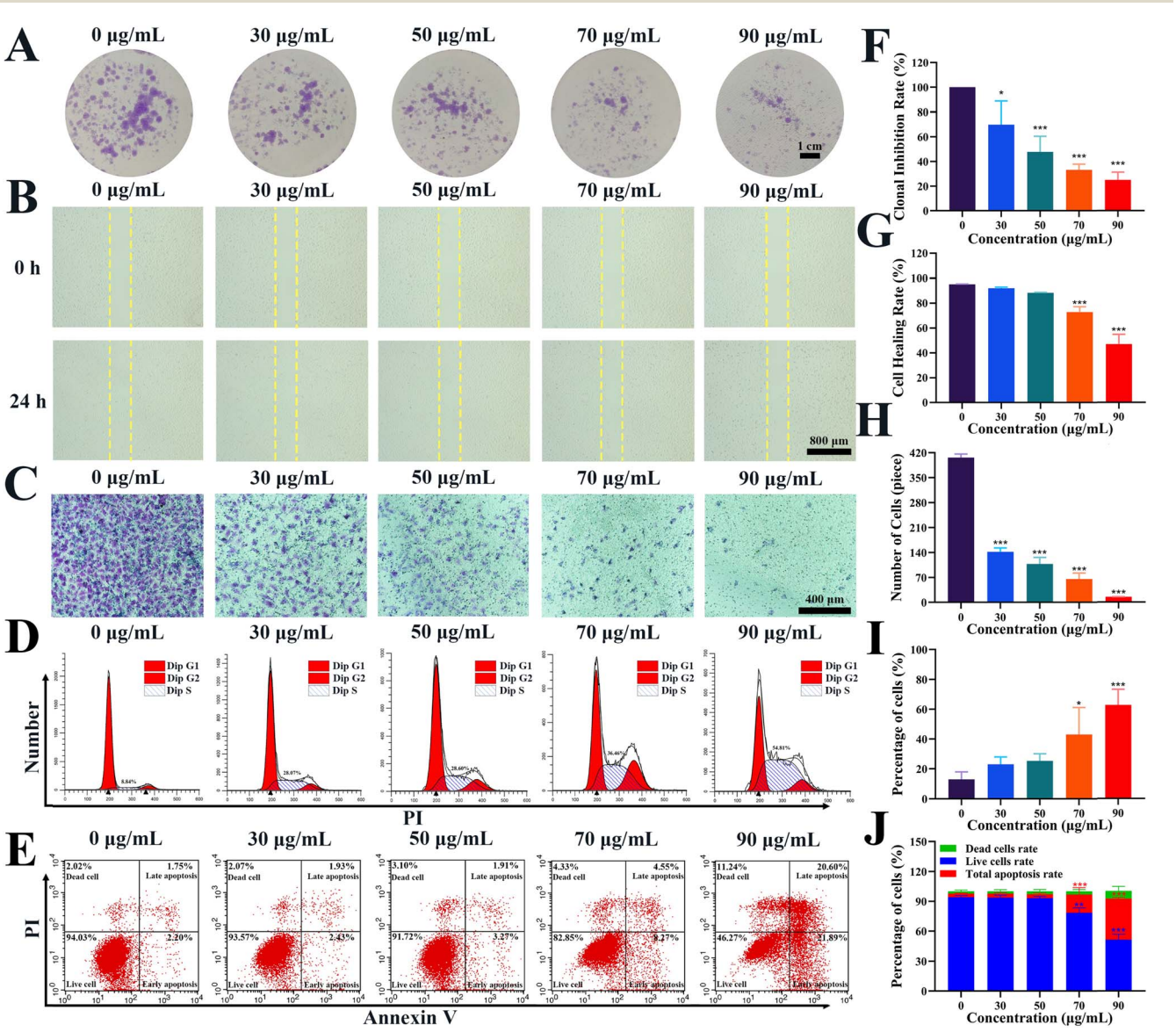

Fig. 3 Effects of the Re-CDs administration on the proliferation, migration, cell cycle and apoptosis of the A498 cells. (A) Images of the colony formation of the 2 weeks-recultured A498 cells after 48 h co-incubation with different concentrations of the Re-CDs. The scale is 1 cm. (B) Microscopic images of wound healing of the A498 cells after 24 h co-incubation with different concentrations of the Re-CDs. The scale bar is 800 μm. (C) Microscopic images of the cell migrations of the A498 cells after 48 h co-incubation with different concentrations of the Re-CDs. The scale bar is 400 μm. (D) The cycle arrest chart of the A498 cells after 48 h co-incubation with different concentrations of the Re-CDs. (E) The apoptosis map of the A498 cells after 48 h co-incubation with different concentrations of Re-CDs. (F) The corresponding statistical histogram of the clonal inhibition rate of (A). (G) The corresponding statistical histogram of the wound healing rate of (B). (H) The corresponding statistical histogram of the migration number of (C). (I) The corresponding statistical chart of the cell cycle arrest of (D). (J) The corresponding statistical histogram of the apoptosis of (E). *$p < 0.05$, **$p < 0.01$ and ***$p < 0.001$, compared to 0 μg mL^{-1}.

migration assay (Fig. 3C). Compared to the control group (Re-CDs, 0 μg mL^{-1}), the mobility of the A498 cells was only ~14.7% ± 0.6% at the Re-CDs concentration of 90 μg mL^{-1} (Fig. 3H). These results showed that the colony-forming ability and migration ability of the A498 cells were significantly inhibited after the Re-CDs treatment (especially at a concentration of 90 μg mL^{-1}) ($p < 0.001$). The cell cycle test results showed that the Re-CDs retarded the A498 cells in the S phase (Fig. 3D and I). With the increase of the administered concentration, the proportion of the A498 cells in the S phase increased in a dose-dependent manner. Compared with the control group (Re-CDs, 0 μg mL^{-1}), the S phase arrest rate of the A498 cells in the highest administered group (Re-CDs, 90 μg mL^{-1}) was ~62.6% ± 10.5% ($p < 0.001$). The results of the apoptosis assay showed that the total apoptosis rate of the A498 cells (including early apoptosis and late apoptosis) increased gradually with the increase of the Re-CDs administration concentration (Fig. 3E and J). Compared with the control group (Re-CDs, 0 μg mL^{-1}), the total apoptosis rate of the highest dose group (Re-CDs, 90 μg mL^{-1}) reached ~41.2% ± 1.2% ($p < 0.001$).

To preliminarily investigate the molecular mechanism of the cell cycle arrest and apoptosis caused by Re-CDs administration, the changes of the reactive oxygen species (ROS), mitochondrial membrane potential (MMP) and Ca^{2+} concentration inside the A498 cells have been detected (Fig. 4). The ROS level in the A498 cells after 48 h co-incubation with Re-CDs at different concentrations (0, 30, 50, 70, and 90 μg mL^{-1}) was detected by 2′,7′-dichlorodihydrofluorescein diacetate (DCFH-DA) as the fluorescent probe. Compared with the control group (Re-CDs, 0 μg mL^{-1}), the Re-CDs administration resulted in significant increases in intracellular ROS levels in the A498 (Fig. 4A and D). When the concentration of the Re-CDs was 90 μg mL^{-1}, the intracellular fluorescence intensity increased by more than 3-fold ($p < 0.001$). This suggests that the Re-CDs can accelerate the production of ROS in the A498 cells, promoting oxidative damage in the cells.[32] When cells undergo oxidative damage, it often leads to abnormal mitochondrial function.[33] The MMP level in the A498 cells was detected by MMP probe JC-1 after incubation with different concentrations (0, 30, 50, 70, and 90 μg mL^{-1}) of the Re-CDs for 48 h (Fig. 4B). With the increase of the administered concentration (30–90 μg mL^{-1}), the intensity of the green fluorescence in the A498 cells gradually increased, and the MMP gradually decreased. When the concentration of the Re-CDs was 90 μg mL^{-1}, the intracellular

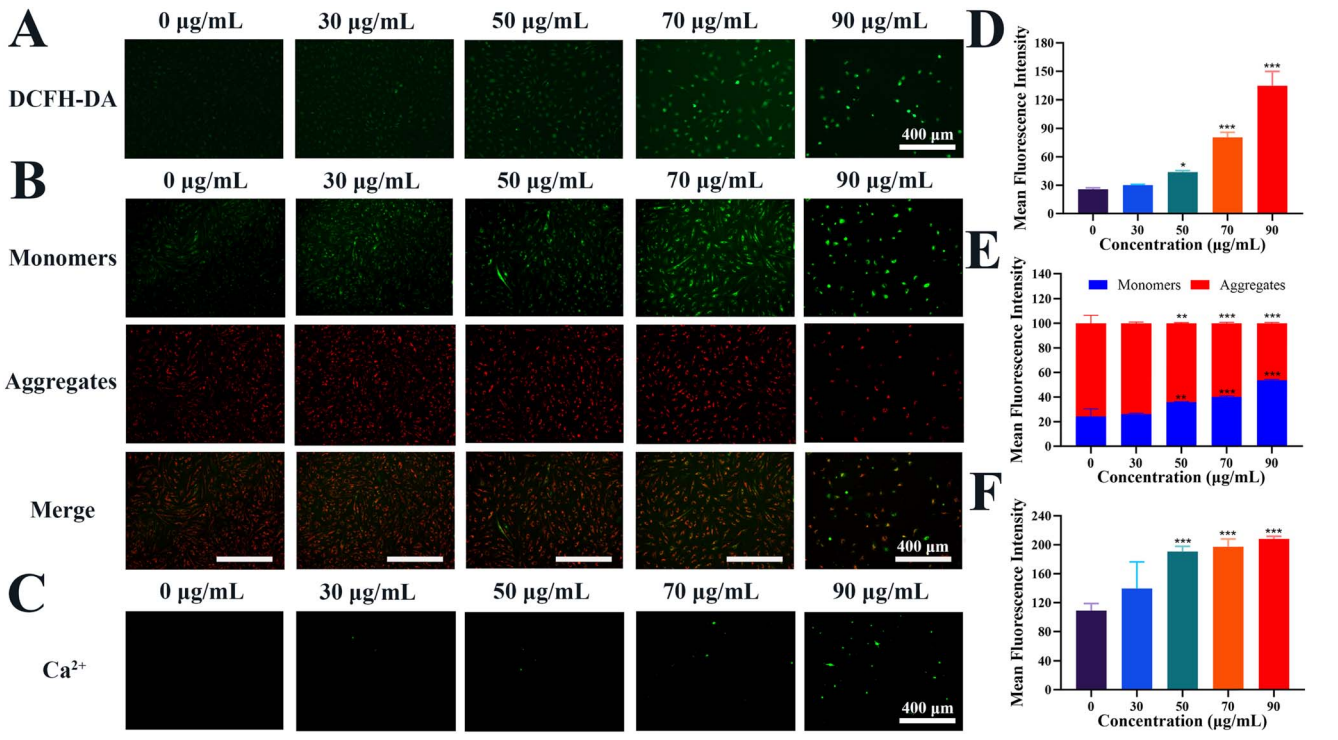

Fig. 4 Effect of the Re-CDs on the ROS level, MMP level, and Ca^{2+} concentration in the A498 cells. (A) Fluorescence images of the changes in ROS levels inside the A498 cells after 48 h of co-incubation with different concentrations of Re-CDs using DCFH-DA (Ex = 470 nm) as the fluorescence probe. (B) Fluorescence images of the changes in MMP levels inside the A498 cells after 48 h of co-incubation with different concentrations of Re-CDs using JC-1 (Ex = 470 and 530 nm) as the fluorescence probe. When the mitochondrial membrane potential of the cell is low, JC-1 is dispersed as a monomer, showing green fluorescence and labeled as monomers. When the mitochondrial membrane potential of the cell is high, JC-1 will aggregate, showing red fluorescence and labeled as aggregates. (C) Fluorescence images of the changes in the Ca^{2+} concentration inside the A498 cells after 48 h of co-incubation with different concentrations of Re-CDs using Fluo-4-AM (Ex = 470 nm) as the fluorescence probe. (D) The corresponding statistical histogram of the intracellular fluorescence intensity of (A). (E) The corresponding statistical histogram of the intracellular fluorescence intensity of (B). (F) The corresponding statistical histogram of the intracellular fluorescence intensity of (C). The scale bar is 400 μm. Compared to 0 μg mL^{-1}, *$p < 0.05$, **$p < 0.01$ and ***$p < 0.001$.

fluorescence intensity increased by ~29.6%, and the MMP level decreased significantly ($p < 0.001$) (Fig. 4E). The administered Re-CDs could promote abnormal mitochondrial function in A498 cells.[34] Furthermore, mitochondrial damage will further promote the production of ROS and the occurrence of apoptosis. Excessive ROS will also further lead to an increase in the release of calcium ions.[35,36] Fluo-4-AM was used to detect changes in the intracellular Ca^{2+} concentration of the A498 after 48 h of co-incubation with different concentrations (0, 30, 50, 70, and 90 μg mL^{-1}) of the Re-CDs. Compared with the control group (Re-CDs, 0 μg mL^{-1}), the green fluorescence intensity, as well as the Ca^{2+} concentration in the A498 cells gradually increased with the increase of the administered concentration (30–90 μg mL^{-1}) (Fig. 4C). The fluorescence intensity in the A498 cells at the Re-CDs concentration of 90 μg mL^{-1} increased by ~90.5% ($p < 0.001$) (Fig. 4F). At the same time, the Hoechst33342/PI staining showed that the intracellular chromatin of the A498 was concentrated and brightened, compared with the control group. The occurrence of apoptosis in the A498 cells was further confirmed (Fig. S7†). These above results indicate that after the Re-CDs administration, the elevated level of ROS in the A498 cells would lead to abnormal mitochondrial function, which in turn led to the decrease in the MMP level and the increase in the Ca^{2+} concentration, and ultimately resulted synergistically in cell cycle arrest and apoptosis.[26,29]

In order to explore in detail the underlying molecular mechanism of the Re-CDs inhibiting the proliferation and promoting apoptosis of the kidney cancer A498 cells, transcriptomics was

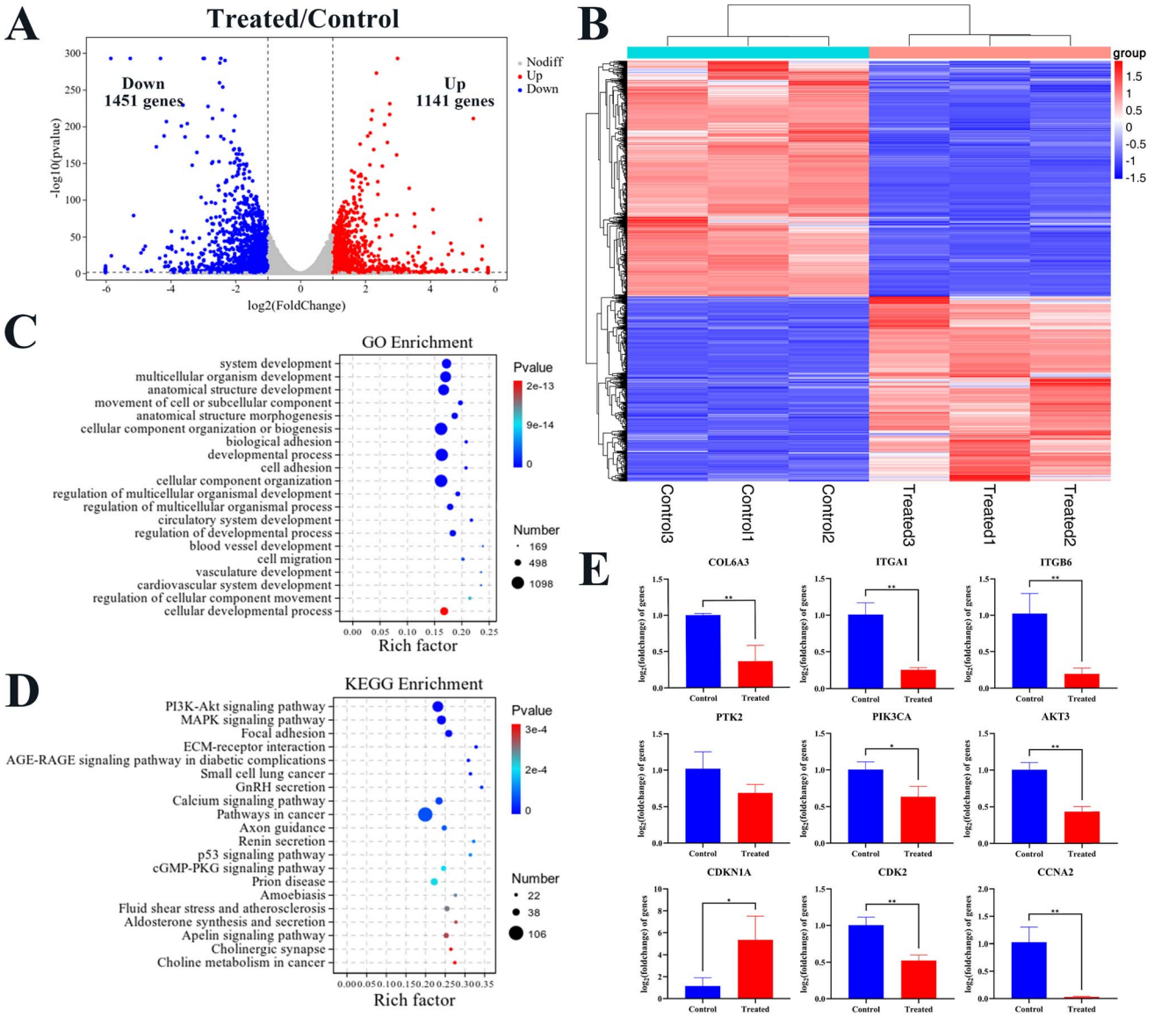

Fig. 5 Transcriptomics to detect the expression and qPCR verification of related genes in A498 cells after Re-CDs administration ($n = 3$). (A) Volcanogram analysis of the DEGs between the control group and the treated group. (B) Cluster heatmap analysis of the DEGs in the control group and the treated group. (C) GO enrichment analysis of the DEGs in the control group and the treated group. (D) KEGG enrichment analysis of the DEGs in the control group and the treated group. (E) qPCR validation histogram of differential genes in PI3K/AKT-related pathways. Compared to the control group, *$p < 0.05$ and **$p < 0.01$.

used to detect the expression and qPCR was used to verify of the related genes in A498 cells after 48 h of co-incubation with the Re-CDs (Fig. 5). The A498 cells with 0 μg mL^{-1} Re-CDs were denoted as the control group, and the A498 cells with 70 μg mL^{-1} Re-CDs were denoted as the treated group. High-throughput RNA sequencing (RNA-seq) was used to evaluate the difference of the related expressed genes between the control group and the treated group under the same condition (Fig. 5A–D). Principal Component Analysis (PCA) showed that the samples of the two groups were highly separated, and there were significant differences (Fig. S8†). As illustrated by the volcano gram of the transcriptome results, differentially expressed genes (DEGs) between the two groups were determined through the DESeq2 algorithm, predicated on fold change ≥2 and adjusted P value <0.05 (Fig. 5A). There was a total of 2592 DEGs, including 1141 up-regulated genes and 1451 down-regulated genes. It showed that the Re-CDs administration could induce significant changes in gene transcription levels in the A498 cells. A significant difference in the mRNA profiles between the treated group and control group is shown in the heatmap (Fig. 5B). The displayed data were in a two-dimensional format, and each value represented a matrix of upregulated (red) and downregulated (blue) genes. Gene Ontology (GO) enrichment analysis was performed to study the biological process, cellular component and molecular function, with the aim of determining the main biological functions performed by the DEGs (Fig. 5C and S9†). These DEGs were mainly concentrated in the system development, multicellular organism development, anatomical structure development, cytoplasm, non-membrane-bounded organelle, intracellular non-membrane-bounded organelle, binding, protein binding, and carbohydrate derivative binding. A pathway enrichment study of the DEGs was performed by the Kyoto Encyclopedia of Genes and Genomes (KEGG) (Fig. 5D). The DEGs were mainly enriched in the PI3K/AKT signaling pathway and the MAPK signaling pathway. Specific primers were selected and designed to verify the RNA-seq screened DEGs through the qPCR (Fig. 5E). It showed that the regulating trends of the nine genes (COL6A3, ITGA1, ITGB6, PTK2, PIK3CA, AKT3, CDKN1A, CDK2 and CCNA2) verified by the qPCR were consistent with the transcriptome test data (Fig. 5A).

Based on the above results, transcriptomics analysis and immunofluorescence were used to detect the expression levels

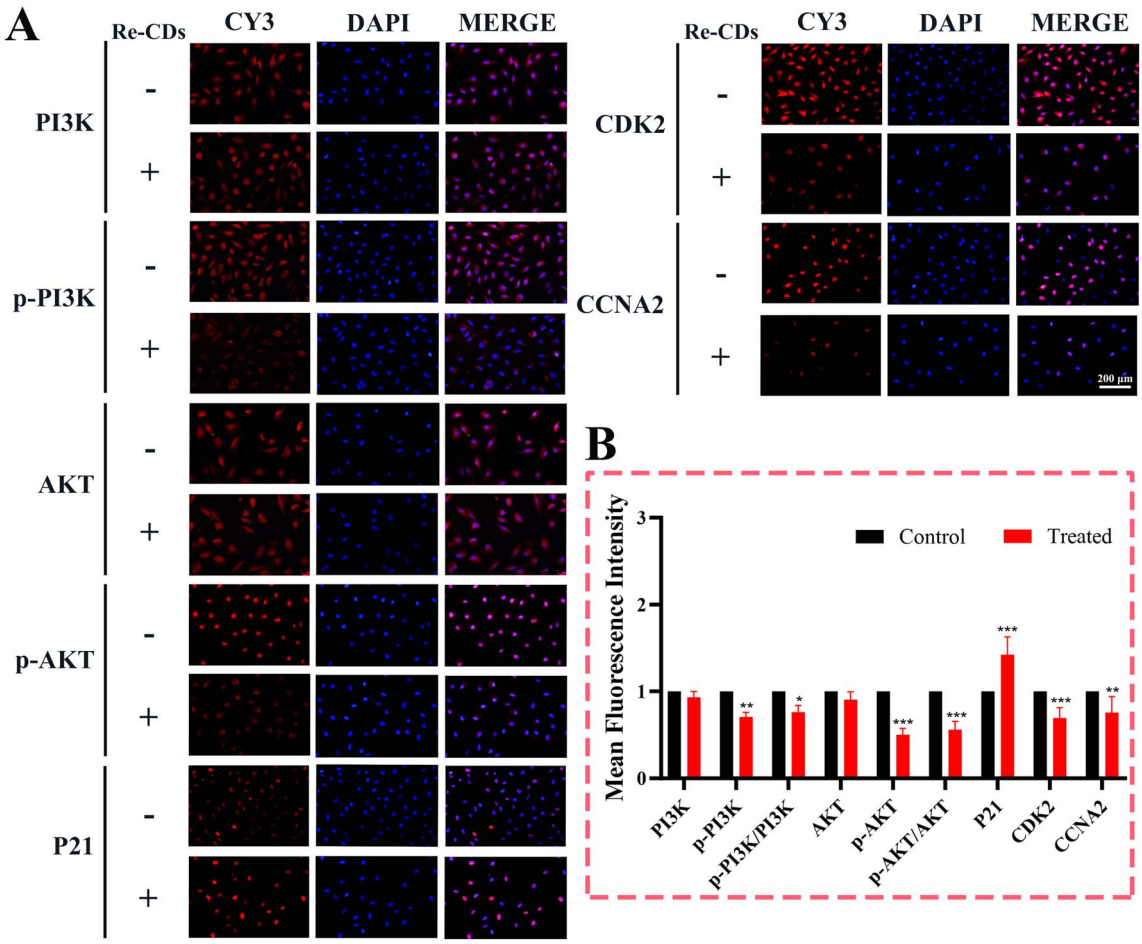

Fig. 6 Immunofluorescence detection was used to evaluate the changes in the expression level of related proteins in the A498 cells after Re-CDs administration. (A) Immunofluorescence images of the related protein expression intracellular A498 after 24 h co-incubation with Re-CDs. "−" represents 0 μg mL^{-1} Re-CDs administration, and "+" represents 90 μg mL^{-1} Re-CDs administration (DAPI, Ex = 360 nm; CY3, Ex = 530 nm). The scale bar is 200 μm. (B) Statistical histogram of the mean fluorescence intensity of the related protein expression detected by immunofluorescence. *p < 0.05, **p < 0.01 and ***p < 0.001.

of the related proteins (PI3K, p-PI3K, AKT, p-AKT, p21, CDK2, and CCNA2) in the PI3K/AKT pathway (Fig. 6). Compared with the normal cultured A498 cells, the expression levels of these key proteins were significantly upregulated or downregulated after the Re-CDs administration (90 μg mL^{-1}). It showed that the Re-CDs could significantly inhibit the expression level of the p-PI3K, further inhibiting the expression level of the downstream protein p-AKT, thereby upregulating the expression level of the cycle regulator p21, and then inhibiting the formation of the CDK2–CCNA2 complex (Fig. 6A and B). It should be noted that the CDK2–CCNA2 complex can promote the transition of the cell cycle from the S phase to the G2 phase. The inhibition of the activity would lead to cell cycle arrest in the S phase, inhibit cell proliferation, and ultimately promote cell apoptosis.[37–40]

A tumor-bearing mouse model using A498 cells as the cancer cells was established to evaluate the inhibitory effect of the Re-CDs on renal cell carcinoma *in vivo* (Fig. 7). All the mice were randomly divided into 4 groups ($n = 5$): control group, model group, 5-FU group, and Re-CDs group. After successful implantation of heterogeneous tumors to the mice in the model group, 5-FU group and Re-CDs group, the experimental period was set to 0–15 days. Tumor-bearing mice were treated with 5-fluorouracil (5-FU group) and Re-CDs (Re-CDs group) (Fig. 7A).[41–44] During the experimental cycle, the body weight of mice in all groups showed an upward trend (Fig. 7B). Apparently, the weight gain trend of mice in the model group and the 5-FU treatment group was lower than that in the control group and the Re-CDs group. The weight gain of mice in the model group was the slowest, indicating that the tumor had a great impact on the mouse bodies. The weight gain of the mice in the 5-FU group was slower. This is likely due to the fact that the chemotherapy drug had great toxic side effects on the mice, while it exerted an inhibitory effect. The weight gain of mice in the Re-CDs group was almost consistent with that in the control group. This indicates that the toxic effect of the Re-CDs on mice was very low. When the inhibitory effect is exerted, the Re-CDs can effectively reduce the burden caused by tumors on mice. The changes in the tumor volume of mice in each group during the experimental period were monitored in real time (Fig. 7C). During the experimental period, the tumor volume of mice in the model group increased significantly. In the later stage, the rate of tumor growth increased much more dramatically. The tumors of mice in the 5-FU group and the Re-CDs group were significantly inhibited at the beginning of the experiment (0–6 days). On the 9th day, the tumor volume of the mice in the 5-FU group increased rapidly and continued until the end of the experiment. At the same time, the tumor volume of the mice in the Re-CDs group still increased slowly. There was a significant difference of the tumor volume of the mice between the model group and the Re-CDs group ($p < 0.001$). Tumor photographs after the experiment showed that the tumors of mice treated with 5-FU and Re-CDs were smaller than those in the untreated model group (Fig. 7D). Similar to the statistical tumor volume, there was a significant difference in the tumor weight of mice between the Re-CDs group and the model group ($p < 0.001$) (Fig. 7E).

After the end of the experimental cycle, the main organs (heart, liver, spleen, lung and kidney) of the mice in each group were H&E stained and analyzed (Fig. S10†). The results showed that the organ cells and tissues of the mice in each group were tightly arranged and had a uniform texture, and there were small obvious lesions. The anticoagulated whole blood of mice in the control group and the Re-CDs group was collected for further routine blood index analysis (Fig. S11†). The blood index

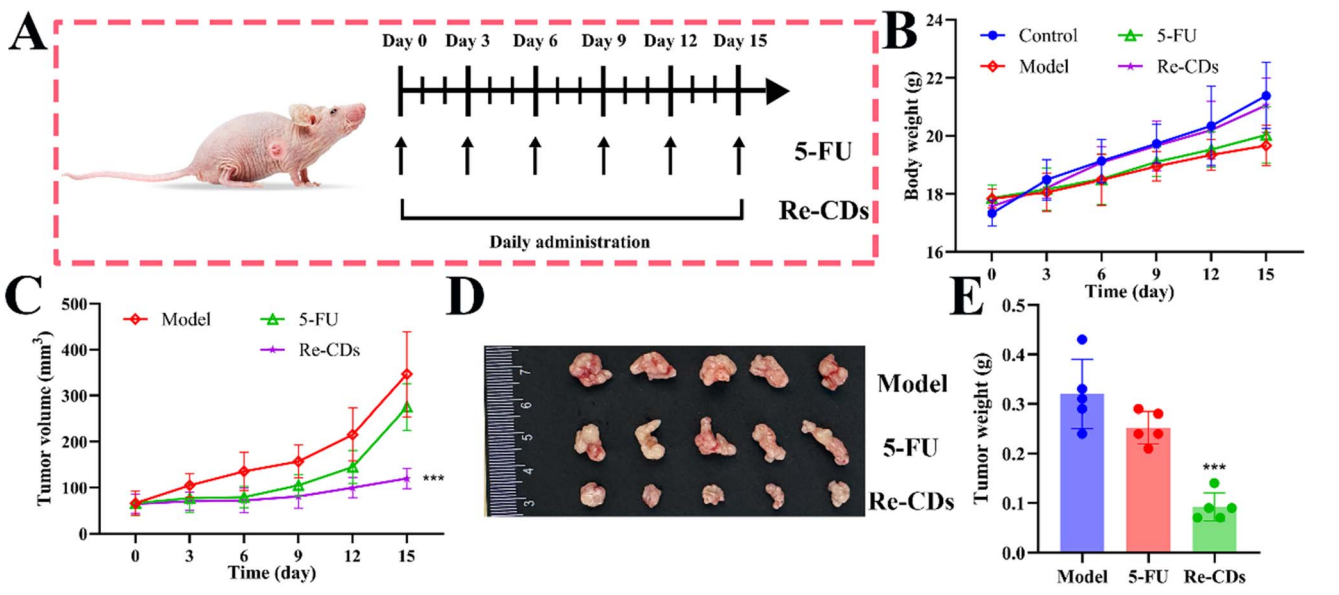

Fig. 7 The anti-renal cell carcinoma activity of the Re-CDs *in vivo* ($n = 5$). (A) Schematic of dosing to mice during an experimental cycle. (B) Statistical chart of the body weight of mice in each group during the experimental cycle. (C) Statistical chart of the tumor volume of mice during the experimental cycle. (D) Photographs of tumors from mice at the end of the treatment (the 15th day). (E) Corresponding statistical histogram of the tumor weight. Compared to the model group, ***$p < 0.001$.

analysis included quantification of hemoglobin (HGB), hemoglobin content (MCH), lymphocytes (LYM), lymphocyte ratio (LYM%), intermediate cells (MID), intermediate cell ratio (MID%), total number of red blood cells (RBC), mean volume of red blood cells (MCV), red blood cell distribution width SD (RDW-SD), red blood cell distribution width CV (RDW-CV), granulocytes (GRAN), granulocyte ratio (GRAN%), total white blood cell count (WBC), total platelet count (PLT), mean platelet volume (MPV), platelet distribution width (PDW), platelet hematocrit (PCT), and platelet large cell ratio (P-LCP). After the Re-CDs treatment, the blood indexes of the mice in the Re-CDs group did not change significantly, compared with that in the control group. Serum samples from mice in the control group and the Re-CDs group were collected for biochemical index analysis (Fig. S12†), which included the key indicators of liver function (alkaline phosphatase (AKP), alanine aminotransferase (ALT), aspartate aminotransferase (AST)), and the key indicators of kidney function (urea nitrogen (BUN), creatinine (CRE), and uric acid (UA)). There was no statistically significant difference in serum indexes between the two groups. The above results showed that the Re-CDs had low biotoxic side effects and good biosafety.

Conclusion

In conclusion, a new high-efficiency and low-toxicity Re-CDs has been prepared *via* hydrothermal method. The size distribution of the Re-CDs was uniform, and concentrated in the 1–4 nm size range. The Re-CDs exhibit good cell membrane permeability and significant inhibition of proliferation and migration ability of the kidney cancer A498 cells. The entry of the Re-CDs into the A498 cells significantly increases the production of intracellular ROS. The excess ROS would induce the functional impairment of mitochondria, the release of Ca^{2+}, and the downregulation of the PI3K/AKT signaling pathway that was abnormally regulated in the tumor cells. The functional impairment of mitochondria and increased intracellular Ca^{2+} concentration further led to the increase in the intracellular ROS levels and the inhibition of the PI3K/AKT signaling pathway. Moreover, the downregulation of the PI3K/AKT signaling pathway would upregulate the expression level of the downstream p21 protein and inhibit the formation of the CDK2–CCNA2 complex, which would lead to cell cycle arrest in the S phase along with the inhibition of cell proliferation. Thus, in conjunction with the abnormal mitochondrial function the Re carbon nanodots could ultimately promote the apoptosis of the A498 cells. Under the same conditions, the Re-CDs have low toxicity to normal cells. This is due to the fact that the excessive proliferation of tumor cells is dependent on the abnormal regulation of the PI3K/AKT signaling pathway. Meanwhile, in the normal cells, the PI3K/AKT signaling pathway is not abnormally activated. Therefore, while achieving the suppression of the tumor cells, the Re-CDs have low toxicity to normal cytotoxicity. The results of the *in vivo* experiments showed that the Re-CDs could significantly inhibit the proliferation of renal cell carcinoma. The tumor growth trend, tumor volume and tumor mass of the mice treated with the Re-CDs were significantly smaller than those in the model group. At the same time, the Re-CDs showed low toxicity and side effects, and good biosafety. Re-CDs can be used as a new low-toxicity and high-efficiency potential nanomedicine for the treatment of kidney cancer.

Methods

Synthesis of the Re-CDs

20.00 mg of ginsenoside Re was placed in a PTFE reactor. Then, 10.00 mL of distilled water was added to the reactor and reacted at 180 °C for 6 h. The solution was then filtered through a 0.22 μm microporous membrane to remove any large insoluble mass. The Re-CDs solution was obtained after centrifugation with a 3500 MW ultrafiltration tube at 5000 rpm three times under 4 °C for 5 min.

Cell viability assay

The A498 cells and LO2 cells were separated incubated in 96-well plates for 12 h. Then, the medium containing different concentrations of the Re-CDs (0, 30, 50, 70 and 90 μg mL^{-1}) was incubated with the cells for 48 h. After the incubation, the medium was discarded and replaced with fresh medium containing the CCK8 reagent (medium : CCK8 = 10 : 1). Subsequently, 110 μL of the reagent was added to each well and the plates were incubated in a 37 °C incubator for 45 min. Their absorbance values at 450 nm were read and the cell viability was calculated.

Hemolysis experiment

Different concentrations (50, 100, 200, 300, 400, and 500 μg mL^{-1}) of the Re-CDs in water, physiological saline (negative control, NC) and water (positive control, PC) were incubated with mouse erythrocytes for 2 h at 37 °C, respectively. The supernatant of each solution was taken and the absorbance at 545 nm was measured.

The hemolysis rate is calculated by the following formula:

$$\text{Hemolysis ratio } (\%) = (A_{\text{sample}} - A_{\text{NC}})/(A_{\text{PC}} - A_{\text{NC}}) \times 100\%$$

Cellular uptake

At 37 °C, the A498 cells were cultured in 24-well plates at a concentration of 2×10^4 per well for 12 h. A volume of 100 μg mL^{-1} of the Re-CDs aqueous solution was added at set concentrations. The A498 cells were co-incubated with the Re-CDs at 37 °C (0, 1, 2, 4, 6, 8, 12, 24, 36, and 48 h), and 4 °C (6 h). Then, the systems were fixed with 4% paraformaldehyde for 30 min. After adding DAPI for staining for 2 min, they were placed under a fluorescence inverted microscope and photographed for observation.

Cell scratch experiment

A498 cells were cultured at 3×10^5 per well in 6-well plates for 12 h. Then, the wound was scratched with a 200 μL tip. The original medium was discarded, and the cells were cultured in low serum MEM medium (2% FBS) containing different concentrations (0, 30, 50, 70, and 90 μg mL^{-1}) of the Re-CDs for 24 h. A microscope was used to take photographs to record the wound healing of the cells.

Colony formation assay and cell migration experiment

The A498 cells were cultured in 6-well plates for 12 h, and incubated with different concentrations (0, 30, 50, 70, and 90 μg mL^{-1}) of the Re-CDs for 48 h.

For the cell cloning experiment, the A498 cells were cultured at 1×10^3 per well in 6-well plates for 2 weeks. A camera was used to obtain photographs.

For the cell migration experiment, A498 cells were cultured at 1×10^5 per well in the upper layer of the transwell chamber. A volume of 600 μL of MEM medium containing 15% FBS was added to the lower layer of the transwell chamber, and the cells continued to incubate for 48 h.

After the end of the culture, the cells were fixed with 4% paraformaldehyde for 30 min, and 0.1% crystal violet was added for staining for 20 min. A microscope was used to obtain the photographs.

Cell apoptosis and cell cycle detected by flow cytometry

The A498 cells were cultured at 1×10^5 per well in 6-well plates for 12 h, and incubated with different concentrations (0, 30, 50, 70, and 90 μg mL^{-1}) of the Re-CDs for 48 h.

For the apoptosis experiment, the collected cells were stained with AV/PI using the BD apoptosis assay kit. After 30 min of incubation in the dark, flow cytometry was used for detection.

For the cell cycle experiment, the cells were resuspended in 70% ethanol (−20 °C). Subsequently, the cells were fixed overnight at 4 °C. PI staining was then performed using a cell cycle kit. After 30 min of incubation in the dark, flow cytometry was used for detection.

Detection of the ROS level, MMP level and Ca^{2+} concentration

The A498 cells were cultured at 1×10^5 per well in 6-well plates for 12 h, and incubated with different concentrations (0, 30, 50, 70, and 90 μg mL^{-1}) of the Re-CDs for 48 h. Staining was performed according to the ROS, MMP, Ca^{2+} detection kits. The cells were then placed under a fluorescence inverted microscope and photographed.

Transcriptomic analysis

The A498 cells without treatment were used as the control group, and the A498 cells with Re-CDs (70 μg mL^{-1}) administration were used as the treated group ($n = 3$). After 48 h of incubation under the same conditions, the two groups of cells were lysed by the Trizol reagent. The total RNA of each group was collected and transcriptome analysis was performed. RNA sequencing and bioinformatic data processing were performed as part of the high-throughput sequencing by the Personal Biotechnology Co., Ltd Shanghai, China.

qRT-PCR verification

The A498 cells without treatment were used as the control group, and the A498 cells with Re-CDs (70 μg mL^{-1}) administration were used as the treated group. After 48 h of incubation under the same conditions, the total RNA of each group was extracted with the Trizol reagent. Reverse transcription and quantitative real-time polymerase chain reaction were performed using the high-capacity reverse transcription kit and the SYBR Green, according to the instructions. All primers used for the PCR are listed in Table S4.†

Immunofluorescence analysis

Re-CDs (90 μg mL^{-1}) were added to a 24-well plate containing 2×10^4 per well A498 cells and incubated for 24 h. The cells were fixed with 4% paraformaldehyde for 30 min. After the cell membrane was permeabilized with Triton X-100, 10% goat serum was added to block for 30 min. After the block, the primary and secondary antibodies were sequentially incubated. The nuclei were stained with DAPI and photographed under a fluorescence microscope.

Anti-renal cell carcinoma activity of the Re-CDs *in vivo*

Four-week-old female BALB/c nude mice were raised in a specific-pathogen-free laboratory. All the mice were randomly divided into 4 groups ($n = 5$): control group, model group, 5-FU group and Re-CDs group. The tumor-bearing mouse model was established by inoculating 100 μL of the A498 cells at a concentration of 1×10^8 mL^{-1} into the right axillary side of the mice. Treatment was initiated and set as the experiment day 0 when the tumor volume of most mice reached ~50–70 mm^3 (volume (mm^3) = (length × $width^2$)/2). The mice in the 5-FU group were administered with the drug at a dosage of 15 mg kg^{-1} every 3 days (intraperitoneal injection).[41] The mice in the Re-CDs group were treated with the drug at a dosage of 10 mg kg^{-1} daily (tail vein injection). The mice in the model group were given an equal volume of normal saline daily (tail vein injection). The body weight of mice in each group was recorded every 3 days. All mice are sacrificed at the 15th day. The heart, liver, spleen, lung and kidney of the mice in each group were collected for H&E staining analysis. Mouse blood was collected for routine blood and biochemical index analysis.

H&E staining analysis

The heart, liver, spleen, lungs and kidneys of the mice were fixed with 4% paraformaldehyde. After the tissues were embedded and sectioned with paraffin, they were stained with the hematoxylin eosin staining solution. The staining photographs were then obtained under a microscope.

Routine blood test

The blood of each mouse was mixed in an anticoagulant tube, and the blood routine index analysis was performed with the routine test instrument.

Biochemical marker detection

The serum of mice in the control group and the Re-CDs group were collected. The biochemical indicators were detected, according to the standard process of the Nanjing Jiancheng Biochemical detection kit, which included alkaline phosphatase (AKP),

alanine aminotransferase (ALT), aspartate aminotransferase (AST), urea nitrogen (BUN), creatinine (CRE), and uric acid (UA).

Statistical analysis

Statistical data were expressed as means ± standard deviation (S.D). Statistical analysis was performed using GraphPad Prism 10.0 software. T-test and one-way ANOVA were used to analyze the differences between data. For all experimental data ($n \geq 3$), $p < 0.05$ were considered statistically significant.

Ethical statement

All procedures were carried out in accordance with the guidelines for the care and use of animals in China, and were approved by the Animal Experiment Ethics Committee of Changchun University of Chinese Medicine (Grant No. 2023567).

Data availability

Supplementary data to this article can be found in the ESI.†

Author contributions

Ning Tian: formal analysis, investigation, methodology, writing – original draft. Xiangling Liu: methodology, validation. Xiaoyu He: writing – review & editing. Ying Liu: formal analysis. Lizhi Xiao: methodology, formal analysis, investigation. Penghui Wang and Di Zhang: data curation. Zhe Zhang: visualization, funding acquisition. Yu Zhao: supervision, project administration. Quan Lin: conceptualization. Changkui Fu: conceptualization. Yingnan Jiang: conceptualization, formal analysis, funding acquisition, writing – review & editing. All authors reviewed the manuscript.

Conflicts of interest

There are no conflicts of interest to declare.

Acknowledgements

The authors are grateful for the support provided by the China Scholarship Council and the Jilin Scientific and Technological Development Programs (20210204176YY, 20240402039GH, and YDZJ202201ZYTS562).

References

1 A. M. Kase, D. J. George and S. Ramalingam, Clear Cell Renal Cell Carcinoma: From Biology to Treatment, *Cancers*, 2023, **15**, 665.
2 W. Xu, M. B. Atkins and D. F. McDermott, Checkpoint inhibitor immunotherapy in kidney cancer, *Nat. Rev. Urol.*, 2020, **17**, 137.
3 G. Manson, A. T. J. Maria, F. Poizeau, F. X. Danlos, M. Kostine, S. Brosseau, S. Aspeslagh, P. Du Rusquec, M. Roger, M. Pallix-Guyot, M. Ruivard, L. Dousset, L. Grignou, D. Psimaras, J. Pluvy, G. Quéré, F. Grados, F. Duval, F. Bourdain, G. Maigne, J. Perrin, B. Godbert, B. I. Taifas, A. Forestier, A. L. Voisin, P. Martin-Romano, C. Baldini, A. Marabelle, C. Massard, J. Honnorat, O. Lambotte and J. M. Michot, Worsening and newly diagnosed paraneoplastic syndromes following anti-PD-1 or anti-PD-L1 immunotherapies, a descriptive study, *J. Immunother Cancer*, 2019, **7**, 337.
4 S. Zhang, X. Chai, G. Hou, F. Zhao and Q. Meng, Platycodon grandiflorum (Jacq.) A. DC.: A review of phytochemistry, pharmacology, toxicology and traditional use, *Phytomedicine*, 2022, **106**, 154422.
5 T. L. Chang, H. Y. Ding and Y. W. Kao, Role of ginsenoside Rd in inhibiting 26S proteasome activity, *J. Agric. Food Chem.*, 2008, **56**, 12011.
6 H. Cheng, J. Liu, Y. Tan, W. Feng and C. Peng, Interactions between gut microbiota and berberine, a necessary procedure to understand the mechanisms of berberine, *J. Pharm. Anal.*, 2022, **12**, 541–555.
7 H. Amekyeh, E. Alkhader, R. Sabra and N. Billa, Prospects of Curcumin Nanoformulations in Cancer Management, *Molecules*, 2022, **27**, 361.
8 E. Garbayo, S. Pascual-Gil, C. Rodríguez-Nogales, L. Saludas, A. Estella-Hermoso de Mendoza and M. J. Blanco-Prieto, Nanomedicine and drug delivery systems in cancer and regenerative medicine, *Wiley Interdiscip. Rev.: Nanomed. Nanobiotechnol.*, 2020, **12**, e1637.
9 G. Nocito, G. Calabrese, S. Forte, S. Petralia, C. Puglisi, M. Campolo, E. Esposito and S. Conoci, Carbon Dots as Promising Tools for Cancer Diagnosis and Therapy, *Cancers (Basel)*, 2021, **13**, 1991.
10 R. Zhang, C. F. Miao, X. Y. Lin, R. J. Lin, X. Q. Deng, J. Y. Huang, Y. Wang, Y. Xu, S. H. Weng and M. Chen, Carbon dots efficiently promote vascularization for enhanced repairing of orthopedic diseases with diabetic mellitus based on nanocatalytic medicine, *Carbon*, 2024, **217**, 118617.
11 D. Li, L. Lin, Y. Fan, L. Liu, M. Shen, R. Wu, L. Du and X. Shi, Ultrasound-enhanced fluorescence imaging and chemotherapy of multidrug-resistant tumors using multifunctional dendrimer/carbon dot nanohybrids, *Bioact. Mater.*, 2020, **6**, 729.
12 C. L. Li, C. M. Ou, C. C. Huang, W. C. Wu, Y. P. Chen, T. E. Lin, L. C. Ho, C. W. Wang, C. C. Shih, H. C. Zhou, Y. C. Lee, W. F. Tzeng, T. J. Chiou, S. T. Chu, J. Cang and H. T. Chang, Carbon dots prepared from ginger exhibiting efficient inhibition of human hepatocellular carcinoma cells, *J. Mater. Chem. B*, 2014, **2**, 4564.
13 L. Tian, H. Ji, W. Wang, X. Han, X. Zhang, X. Li, L. Guo, L. Huang and W. Gao, Mitochondria-targeted pentacyclic triterpenoid carbon dots for selective cancer cell destruction *via* inducing autophagy, apoptosis, as well as ferroptosis, *Bioorg. Chem.*, 2023, **130**, 106259.
14 Y. Jiang, L. Xiao, J. Wang, T. Tian, G. Liu, Y. Zhao, J. Guo, W. Zhang, J. Wang, C. Chen, W. Gao and B. Yang, Carbon nanodots constructed by ginsenosides and their high inhibitory effect on neuroblastoma, *J. Nanobiotechnol.*, 2023, **21**, 244.

15 A. Glaviano, A. S. C. Foo, H. Y. Lam, K. C. H. Yap, W. Jacot, R. H. Jones, H. Eng, M. G. Nair, P. Makvandi, B. Geoerger, M. H. Kulke, R. D. Baird, J. S. Prabhu, D. Carbone, C. Pecoraro, D. B. L. Teh, G. Sethi, V. Cavalieri, K. H. Lin, N. R. Javidi-Sharifi, E. Toska, M. S. Davids, J. R. Brown, P. Diana, J. Stebbing, D. A. Fruman and A. P. Kumar, PI3K/AKT/mTOR signaling transduction pathway and targeted therapies in cancer, *Mol. Cancer*, 2023, **22**, 138.

16 H. Li, J. Hu, S. Wu, L. Wang, X. Cao, X. Zhang, B. Dai, M. Cao, R. Shao, R. Zhang, M. Majidi, L. Ji, J. V. Heymach, M. Wang, S. Pan, J. Minna, R. J. Mehran, S. G. Swisher, J. A. Roth and B. Fang, Auranofin-mediated inhibition of PI3K/AKT/mTOR axis and anticancer activity in non-small cell lung cancer cells, *Oncotarget*, 2016, **7**, 3548.

17 C. Yang, Y. Gong, M. Deng, Y. Ling, J. Wang and Y. Zhou, Discovery of a photosensitizing PI3K inhibitor for tumor therapy: design, synthesis and *in vitro* biological evaluation, *Bioorg. Med. Chem. Lett.*, 2023, **94**, 129459.

18 L. Zhu, B. Derijard, K. Chakrabandhu, B. S. Wang, H. Z. Chen and A. O. Hueber, Synergism of PI3K/Akt inhibition and Fas activation on colon cancer cell death, *Cancer Lett.*, 2014, **354**, 355.

19 M. S. Ayoup, I. Shawki, H. Abdel-Hamid, D. A. Ghareeb, A. Masoud, M. F. Harras, M. El-Atawy, N. S. Alharbi and M. M. F. Ismail, Targeting EGFR/PI3K/AKT/mTOR signaling in lung and colon cancers: synthesis, antitumor evaluation of new 1,2,4-oxdiazoles tethered 1,2,3-triazoles, *RSC Adv.*, 2024, **14**, 16713.

20 J. Liu, N. Tang, N. Liu, P. Lei and F. Wang, Echinacoside inhibits the proliferation, migration, invasion and angiogenesis of ovarian cancer cells through PI3K/AKT pathway, *J. Mol. Histol.*, 2022, **53**, 493.

21 P. Patel, D. Umapathy, S. Manivannan, V. M. Nadar, R. Venkatesan, V. A. Joseph Arokiyam, S. Pappu and K. Ponnuchamy, A doxorubicin-platinum conjugate system: impacts on PI3K/AKT actuation and apoptosis in breast cancer cells, *RSC Adv.*, 2021, **11**, 4818.

22 T. Wu, Y. Chen, C. Yang, M. Lu, F. Geng, J. Guo, Y. Pi, Y. Ling, J. Xu, T. Cai, L. Lu and Y. Zhou, Systematical Evaluation of the Structure-Cardiotoxicity Relationship of 7-Azaindazole-based PI3K Inhibitors Designed by Bioisosteric Approach, *Cardiovasc. Toxicol.*, 2023, **23**, 364.

23 C. Yang, M. Wang, Y. Gong, M. Deng, Y. Ling, Q. Li, J. Wang and Y. Zhou, Discovery and identification of a novel PI3K inhibitor with enhanced CDK2 inhibition for the treatment of triple negative breast cancer, *Bioorg. Chem.*, 2023, **140**, 106779.

24 C. Yang, Y. Chen, T. Wu, Y. Gao, X. Liu, Y. Yang, Y. Ling, Y. Jia, M. Deng, J. Wang and Y. Zhou, Discovery of N-(2-chloro-5-(3-(pyridin-4-yl)-1H-pyrazolo[3,4-b]pyridin-5-yl) pyridin-3-yl)-4-fluorobenzenesulfonamide (FD274) as a highly potent PI3K/mTOR dual inhibitor for the treatment of acute myeloid leukemia, *Eur. J. Med. Chem.*, 2023, **258**, 115543.

25 C. Yang, M. Lu, Y. Chen, R. Xiang, T. Qiu, Y. Jia, Y. Yang, X. Liu, M. Deng, Y. Ling and Y. Zhou, Development of anti-breast cancer PI3K inhibitors based on 7-azaindole derivatives through scaffold hopping: design, synthesis and *in vitro* biological evaluation, *Bioorg. Chem.*, 2021, **117**, 105405.

26 C. Yang, C. Xu, Z. Li, Y. Chen, T. Wu, H. Hong, M. Lu, Y. Jia, Y. Yang, X. Liu, M. Deng, Z. Chen, Q. Li, Y. Ling and Y. Zhou, Bioisosteric replacements of the indole moiety for the development of a potent and selective PI3Kδ inhibitor: design, synthesis and biological evaluation, *Eur. J. Med. Chem.*, 2021, **223**, 113661.

27 C. Tao, J. Zhang, J. Wang and Y. Le, Ginsenoside Drug Nanocomposites Prepared by the Aerosol Solvent Extraction System for Enhancing Drug Solubility and Stability, *Pharmaceutics*, 2018, **10**, 95.

28 J. Xin, M. Song, X. Liu, H. Zou, J. Wang, L. Xiao, Y. Jia, G. Zhang, W. Jiang, M. Lei, Y. Yang and Y. Jiang, A new strategy of using low-dose caffeic acid carbon nanodots for high resistance to poorly differentiated human papillary thyroid cancer, *J. Nanobiotechnol.*, 2024, **22**, 571.

29 B. Wang and S. Lu, The light of carbon dots: From mechanism to applications, *Matter*, 2022, **5**, 110.

30 X. Chu, K. Li, H. Guo, H. Zheng, S. Shuda, X. Wang, J. Zhang, W. Chen and Y. Zhang, Exploration of Graphitic-C3N4 Quantum Dots for Microwave-Induced Photodynamic Therapy, *ACS Biomater. Sci. Eng.*, 2017, **3**, 1836.

31 Y. W. Bao, X. W. Hua, Y. H. Li, H. R. Jia and F. G. Wu, Endoplasmic reticulum-targeted phototherapy using one-step synthesized trace metal-doped carbon-dominated nanoparticles: laser-triggered nucleolar delivery and increased tumor accumulation, *Acta Biomater.*, 2019, **88**, 462.

32 Y. Hong and D. Fan, Ginsenoside Rk1 induces cell cycle arrest and apoptosis in MDA-MB-231 triple negative breast cancer cells, *J. Funct. Foods*, 2019, **418**, 22.

33 D. B. Zorov, M. Juhaszova and S. J. Sollott, Mitochondrial reactive oxygen species (ROS) and ROS-induced ROS release, *Physiol. Rev.*, 2014, **94**, 909.

34 D. Chaoui, A. M. Faussat, P. Majdak, R. Tang, J. Y. Perrot, S. Pasco, C. Klein, J. P. Marie and O. Legrand, JC-1, a sensitive probe for a simultaneous detection of P-glycoprotein activity and apoptosis in leukemic cells, *Cytometry B Clin. Cytom.*, 2006, **70**, 189.

35 A. González, A. Schmid, G. M. Salido, P. J. Camello and J. A. Pariente, XOD-catalyzed ROS generation mobilizes calcium from intracellular stores in mouse pancreatic acinar cells, *Cell Signal*, 2002, **14**, 153.

36 L. Liu, X. Sun, Y. Guo and K. Ge, Evodiamine induces ROS-Dependent cytotoxicity in human gastric cancer cells *via* TRPV1/Ca^{2+} pathway, *Chem.-Biol. Interact.*, 2022, **351**, 109756.

37 J. Tak, A. Sabarwal, R. K. Shyanti and R. P. Singh, Berberine enhances posttranslational protein stability of p21/cip1 in breast cancer cells *via* down-regulation of Akt, *Mol. Cell. Biochem.*, 2019, **458**, 49.

38 Y. Jin, Z. Wang, N. Aobulikasimu, Y. Hu, Z. Zhang, H. Lv, Y. Mu, Y. Jiang, L. Han and X. Huang, Discovery, synthesis, and cytotoxic evaluation of isoquinolinequinones produced by *Streptomyces albidoflavus* derived from lichen, *RSC Adv.*, 2023, **13**, 34670.

39 C. Zhang, Y. Quan, L. Yang, Y. Bai and Y. Yang, 6-Methoxyflavone induces S-phase arrest through the CCNA2/CDK2/p21CIP1 signaling pathway in HeLa cells, *Bioengineered*, 2022, **13**, 7277.

40 J. Li, L. Shang, F. Zhou, S. Wang, N. Liu, M. Zhou, Q. Lin, M. Zhang, Y. Cai, G. Chen and S. Yang, Herba Patriniae and its component Isovitexin show anti-colorectal cancer effects by inducing apoptosis and cell-cycle arrest *via* p53 activation, *Biomed. Pharmacother.*, 2023, **168**, 115690.

41 D. Luo, X. Liu, L. Jiang, Z. Guo, Y. Lv, X. Tian, X. Wang, S. Cui, S. Wan, X. Qu, X. Xu and X. Li, Rational Design, Synthesis, and Biological Evaluation of Novel S1PR2 Antagonists for Reversing 5-FU-Resistance in Colorectal Cancer, *J. Med. Chem.*, 2022, **65**, 14553.

42 Y. Y. Liang, S. Bacanu, L. Sreekumar, A. D. Ramos, L. Dai, M. Michaelis, J. Cinatl, T. Seki, Y. Cao, C. R. Coffill, D. P. Lane, N. Prabhu and P. Nordlund, CETSA interaction proteomics define specific RNA-modification pathways as key components of fluorouracil-based cancer drug cytotoxicity, *Cell Chem. Biol.*, 2022, **29**, 572.

43 M. Hong, Y. Du, D. Chen, Y. Shi, M. Hu, K. Tang, Z. Hong, X. Meng, W. Xu, G. Wu, Y. Yao, L. Chen, W. Chen, C. Y. Lau, L. Sheng, T. H. Zhang, H. Huang, Z. Fang, Y. Shen, F. Sun, J. Qian, H. Qu, S. Zheng, S. Zhang, K. Ding and R. Sun, Martynoside rescues 5-fluorouracil-impaired ribosome biogenesis by stabilizing RPL27A, *Sci. Bull. (Beijing).*, 2023, **68**, 1662.

44 M. Miyake, S. Anai, K. Fujimoto, S. Ohnishi, M. Kuwada, Y. Nakai, T. Inoue, A. Tomioka, N. Tanaka and Y. Hirao, 5-fluorouracil enhances the antitumor effect of sorafenib and sunitinib in a xenograft model of human renal cell carcinoma, *Oncol. Lett.*, 2012, **3**, 1195.